# Laboratory-based bidirectional reflectance distribution functions of radiometric tarps

Georgi T. Georgiev[1,*] and James J. Butler[2]

[1]Science Systems and Applications, Incorporated, Lanham, Maryland 20706, USA

[2]NASA Goddard Space Flight Center, Code 614.4, Greenbelt, Maryland 20771, USA

*Corresponding author: georgi.t.georgiev@nasa.gov

Laboratory-based bidirectional reflectance distribution functions (BRDFs) of radiometric tarp samples used in the vicarious calibration of Earth remote sensing satellite instruments are presented in this paper. The results illustrate the BRDF dependence on the orientation of the tarps' weft and warp threads. The study was performed using the GSFC scatterometer at incident zenith angles of 0°, 10°, and 30°; scatter zenith angles from 0° to 60°; and scatter azimuth angles of 0°, 45°, 90°, 135°, and 180°. The wavelengths were 485 nm, 550 nm, 633 nm, and 800 nm. The tarp's weft and warp dependence on BRDF is well defined at all measurement geometries and wavelengths. The BRDF difference can be as high as 8% at 0° incident angle and 12% at 30° incident angle. The fitted BRDF data show a very small discrepancy from the measured ones. New data on the forward and backscatter properties of radiometric tarps are reported. The backward scatter is well pronounced for the white samples. The black sample has well-pronounced forward scatter. The provided BRDF characterization of radiometric tarps is an excellent reference for anyone interested in using tarps for radiometric calibrations. The results are NIST traceable. © 2008 Optical Society of America

*OCIS codes:* 290.1483, 120.3940, 120.4800, 120.5820, 120.0280.

## 1. Introduction

The ability to monitor, understand, and predict the Earth's climate and environmental processes depends on the quality of data from Earth's remote sensing instruments. The global nature of Earth's processes requires consistent long-term calibration of all instruments involved in data retrieval [1]. The bidirectional reflectance distribution function (BRDF) defines the directional reflection characteristics of an optical surface. It provides the reflectance of a target in a specific direction as a function of illumination and viewing geometry. The BRDF is a function of wavelength and reflects the structural and optical properties of the surface. Various space and airborne radiometric and imaging remote sensing instruments use diffuse scatter plates as calibration sources requiring preflight BRDF calibration measurements

[2,3]. Onboard diffusers are used to trend on-orbit instrument radiance or reflectance calibration. Laboratory-based diffusers are used for preflight instrument radiance calibrations. BRDF measurements of natural targets are also used for remote sensing characterization of vegetation canopies and soils [4], oceans [5], or especially large pollution sources [6].

The data reported in this study are intended to more completely describe the BRDF of radiometric tarp samples, with particular interest on the effect of tarp weft and warp thread orientation. This study was done in support of the commercial remote sensing radiometric characterization program of IKONOS multispectral imagery at NASA's Stennis Space Center, from which the samples were obtained [7,8]. The samples are witness pieces from larger chemically treated field-deployed radiometric canvas tarps used as reference reflectance standards in remote sensing characterizations. The radiometric tarps were also used to perform spatial characterizations measuring

the sensors ability to image an edge formed by using two contrasting tarps. The tarps are manufactured with strict specifications; they are large enough to characterize the spatial characteristics of 1 m ground sample distance (GSD) class imagery. The targets can easily be deployed over alternative sites; the proper care at deployment being of great importance. The accuracy of such tarp-based field calibrations depends on an accurate knowledge of the tarps laboratory measured BRDF at the different geometries of source and scatter zenith and azimuth angles. The reported data are traceable to NIST's Spectral Tri-function Automated Reference Reflectometer (STARR) [9] via test standards.

## 2. BRDF Background

The BRDF definition and derivation are credited to Nicodemus *et al.* [10] who examined the problem of defining and measuring the scatter of diffuse and specular optical materials. Following his concept, the scatter defining geometry is shown in Fig. 1, where the subscripts $i$ and $s$ refer to incident and scatter quantities, respectively. He also assumed that all scatter comes from the sample surface and none from the bulk. He defined the BRDF in radiometric terms as the ratio of the surface radiance $L_s$ scattered by a surface into the direction $(\theta_s, \phi_s)$ to the incident surface irradiance $E_i$ incident on a unit area of the surface at a particular wavelength:

$$\text{BRDF} = \frac{\mathrm{d}L_s(\theta_i, \phi_i, \theta_s, \phi_s; E_i)}{\mathrm{d}E_i(\theta_i, \phi_i)}, \qquad (1)$$

where the subscripts $i$ and $s$ denote incident and scattered, respectively, $\theta$ the zenith, and $\varphi$ the azimuth angles.

Nicodemus further assumed that the beam has a uniform cross section, the illuminated area on the sample is isotropic, and all scatter comes from the sample surface. In practice, we are dealing with real samples' surfaces which are not isotropic and the op-
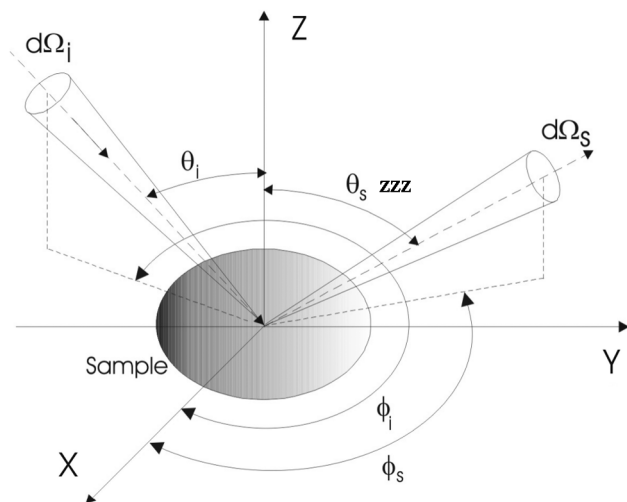
tical beams used to measure the reflectance are not perfectly uniform. Hence from the practical considerations the BRDF can be defined, as presented by Stover [11], as the scattered power per unit solid angle normalized by the incident power and the cosine of the detector zenith angle. It is expressed in terms of incident power, scattered power, and the geometry of incident and reflected light:

$$\text{BRDF} = \frac{P_s/\Omega}{P_i \cos\theta_s}, \qquad (2)$$

where $P_i$ is the incident power, $P_s$ is the scatter power, $\theta_s$ is the detector zenith angle, and $\Omega$ is the solid angle determined by the area of detector aperture, $A$, and the distance from the sample surface to the limiting aperture at the detector assembly, $R$, or $\Omega = A/R$.

We are using the above BRDF expression [Eq. (2)] as it allows for bulk scatter in addition to surface scatter and permits nonuniform incident beam profiles. BRDF has units of inverse steradians and can range from very small numbers (e.g., off-specular black samples) to very large values (e.g., highly reflective samples at specular reflectance). The BRDF is often called cosine-corrected, when the $\cos\theta_s$ factor is not included. We are following the Nicodemus–Stover convention through this study; however care is required as some publications do not follow it. For example, although the remote sensing community follows the Nicodemus approach as a complete description of the BRDF of a surface, Eq. (1), it prefers to use the van de Hulst defined bidirectional reflection function (BRF) in dealing with actual measurements under natural conditions:

$$\text{BRF} = \frac{\pi I_\lambda(\theta, \theta_0, \Phi)}{\mu_0 F_\lambda}, \qquad (3)$$

where $I_\lambda$ is a reflected intensity, $F_\lambda$ is the solar flux density incident on the top of the atmosphere, $\theta$ and $\theta_0$ are, respectively, the scatter zenith and incident zenith angles, $\Phi$ is the azimuth angle between the scatter and incident light directions, and $\mu_0 = \cos\theta_0$. The BRF is dimensionless, normalized to the reference illumination irradiance.

## 3. Measurement Setup and Samples

The radiometric tarp samples were studied in the Diffuser Calibration Facility at NASA's Goddard Space Flight Center (GSFC) using the facility's scatterometer. The scatterometer, located in a class 10000 laminar flow cleanroom, is capable of measuring the BRDF or bidirectional transmissive distribution function (BTDF) of a wide range of sample types including white diffusers, gray-scale diffusers, black painted or anodized diffusers, polished or roughened metal surfaces, clean or contaminated mirrors, transmissive diffusers, liquids, and granular solids. The operational spectral range of the instrument is from 230 to 900 nm. The scatterometer facilitates compu-



Fig. 1. BRDF geometry of incident and reflected elementary beams after Nicodemus.

terized measurements at selected incident and scattered geometries and wavelengths for complete data acquisition. The measurement uncertainty, $\Delta_{\mathrm{BRDF}}$,

$$(\Delta_{\mathrm{BRDF}})^2 = 2(\Delta_{\mathrm{NS}})^2 + 2(\Delta_{\mathrm{LIN}})^2 + (\Delta_{\mathrm{SLD}})^2$$
$$+ [\Delta_{\theta s}\tan(\theta_s)]^2, \qquad (4)$$

depends on several instrument variables. It was subsequently evaluated by Schiff *et al.* [12] and Cady *et al.* [13] in accordance with NIST guidelines [14] to be less than 1% standard uncertainty. The main sources of uncertainty are considered independent. They are: (1) signal to noise ratio, $\Delta_{\mathrm{NS}}$; (2) nonlinearity of the electronics, $\Delta_{\mathrm{LIN}}$; (3) receiver solid angle, $\Delta_{\mathrm{SLD}}$; (4) the total scatter angle error, $\Delta_{\theta s}$; and (5) the error of the receiver scatter angle, $\theta_s$.

The samples in this study are small witness samples of the large tarps used in the vicarious calibration efforts of Stennis Space Center. Three measurements were performed at each wavelength, scatter geometry, and polarization state of the incident light and the average is reported. The measured data were found to be consistent to within 0.5%. The high accuracy laboratory BRDF is provided to serve as a reference to the field observations and to deal with all wrinkle and terrain roughness.

The scatterometer can perform in-plane and out-of-plane BRDF and BTDF measurements, and 8° directional/hemispherical measurements. It consists of a vertical optical source table, a sample stage, a detector goniometer, and a computer system for positioning control, data collection and analysis. Figure 2 shows the instrument's optical layout. The optical table can be rotated around its horizontal axis located at the table center to change the incident angle, $\theta_i$, relative to the sample normal. The optical source table contains two possible light sources—a 75 W xenon short-arc lamp coupled to a Chromex 250SM scanning monochromator and a He–Ne laser. Although not shown on Fig. 2, additional laser sources are possible. The xenon lamp assembly is compact and generates an output beam focused on a monochromator entrance slit. A filter wheel is attached to the exit slit to block higher order spectra. Spherical and flat mirrors focus the output monochromatic beam on a fixed aperture. The optical beam is then directed to the sample surface by one spherical and two flat mirrors. The incident light is linearly polarized by a Glan–Thompson polarizer. The optical path for the laser source is simpler. Flat mirrors direct the laser beam to the sample. The incident beam is collimated by two lenses and linearly polarized by a different Glan–Thompson polarizer. When measurements are made with the xenon short-arc lamp source, the folding mirror and the polarizer for the laser beam, shown in Fig. 2 by a dashed line, which would block the xenon lamp beam, are removed.

Figure 3 shows the goniometer mechanism of the scatterometer. The scattered light from the sample is
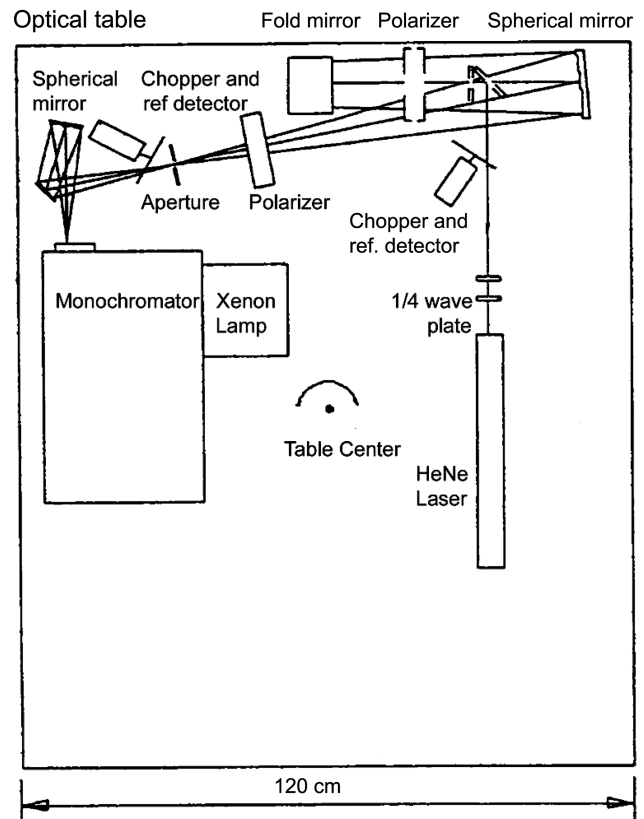


Fig. 2. NASA–GSFC scatterometer vertical optical table with the axis of rotation at the table center.
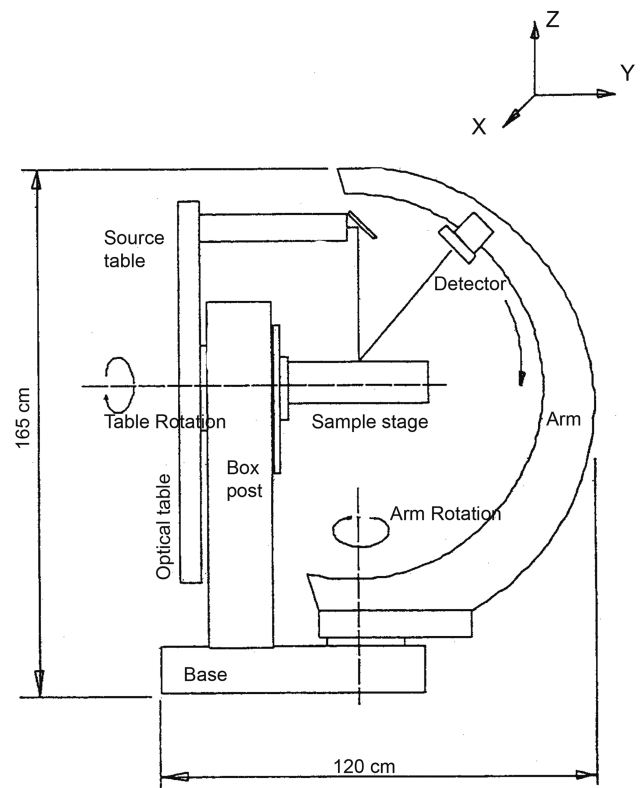


Fig. 3. NASA–GSFC scatterometer goniometer with the optical table and the axis of rotation of the optical table, and the axis of rotation of goniometer arm.

collected using an ultraviolet-enhanced silicon photodiode detector with output fed to a computer-controlled lock-in amplifier. The sample is mounted on a stage in the horizontal plane. The sample stage allows proper positioning of the sample with respect to the incident beam. It can be moved in $X$, $Y$ and $Z$ linear directions using three motors. The sample stage provides sample rotation in the horizontal plane around the Z axis enabling changes in the incident azimuth angle, $\varphi_i$. Sample stage leveling is adjustable using two manual micrometers. Various holders are available to support samples of different sizes, shapes, and thicknesses. Samples can be as large as 45 cm square and up to 4.5 kg in weight. However, larger and heavier samples can be measured by using an appropriate external sample stage.

The position of the detector assembly is determined by the scatter zenith and scatter azimuth angles. The detector assembly can be rotated around the vertical, $Z$, and horizontal, $X$, $Y$ axes of the goniometer. As shown in Fig. 3, the detector moves along the arc providing the ability to make scatter measurements as a function of the scatter zenith angle, $\theta_s$. The arc rotates 180° around the vertical Z axis which determines the scatter azimuth angle, $\varphi_s$. The center of the illuminated spot on the surface of the sample must be positioned at the cross point of the three perpendicular goniometer rotation axes, $X$, $Y$, and $Z$, coinciding with the center of a sphere with radius equal to the distance between that point and the detector's assembly cover aperture.

The operation of the scatterometer is fully computerized. Custom software was developed to control all motion, data acquisition, and data analysis. The optical beams are mechanically chopped and a lock-in data acquisition technique is used. The electronics consists of a motion control module and a lock-in-amplifier. A custom preamp embedded into the detector housing was also designed and built.

The Diffuse Calibration Facility has participated in several round-robin [15] measurement campaigns with domestic and foreign institutions. It has supported a number of NASA and international remote sensing Earth and space projects. The facility has characterized many types of samples including Spectralon [16], Aluminum diffusers, Barium Sulfate, optical elements, Martian regolith simulant [17], natural samples as vegetation and soil [18], etc.

## 4. Experiment

The four tarp samples being studied are all 10 cm × 10.5 cm cut along the weft and warp thread directions. The warp and weft are weaving terms. The warp is the set of lengthwise yarns across which the weft is shuttled back and forth to create a woven fabric. The samples are of similar material structure, possessing a highly regular wavelike structure but with different reflectance. The surface structure of the samples is shown on a microscopic image of tarp sample 1 in Fig. 4. The tarps were made of woven polyester duck with a protective silicone pigmented
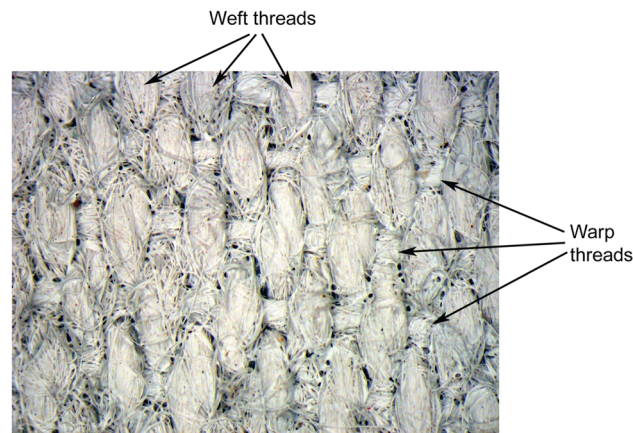


Fig. 4. (Color online) Microscopic image of tarp sample 1, where the warp threads are horizontal and weft threads are vertical.

coating. The samples were mounted flat on the scatterometer sample stage. The illuminated area depends on the incident angle. It varies from 16 mm in diameter at 0° incident angle to an ellipse with a long axis of 28 mm at 30° incident angle.

The bidirectional reflectance distribution of any sample strongly depends on the direction of the incident light on the sample and the detector's position as determined by the scatter zenith and scatter azimuth angles. The incident light along the sample normal describes the sample's bidirectional reflectance distribution at normal incidence, while the incident light at angles other than normal describes the bidirectional reflectance distribution at nonnormal incidence. The incident and scatter angles of this study were chosen by Stennis Space Center based on the illumination geometries of their vicarious airborne calibrations. Both in-the-principal-plane and out-of-the-principal-plane scans were performed hereafter referred to as in-plane and out-of-plane. The incident angles (i.e., source zenith) were 0°, 10°, and 30°; the source azimuth angle was fixed at 4°. The latter is a result of IKONOS orbital mechanics and the need to have a tilted edge that can help to create an edge response relatively free from aliasing effects. The in-plane scans are at scatter azimuth angles of 0° and 180°. The out-of-plan scans were at scatter azimuth angles of 45°, 90°, and 135°. All the scans were performed at scatter zenith angles from 0° to 60° in 5° steps. The wavelengths were 485, 550, 633, and 800 nm with a spectral bandwidth of 12 nm. The detector field-of-view (FOV) was centered on the samples for all measurements. We used the underfilled BRDF measurement technique, meaning the illuminated area on the sample was always smaller than the detector FOV. All measurements in the current study were made for polarizations of the incident beam both parallel and perpendicular to the plane of incidence. The BRDF values for both polarizations were then averaged to yield the BRDF for unpolarized incident radiant flux, and the values of the unpolarized scattering case are reported in this paper.

The 8° directional/hemispherical reflectance of the same samples was also measured. The 8° integrating sphere is a separate accessory to the scatterometer. The sphere collects and spatially integrates the scattered optical radiation. The sphere interior is Spectralon with a typical reflectance of 94% to 99% from the UV to the NIR. The sphere was designed with four ports to accommodate the sample, the detector, and the entry of the incident light. A fourth port is a spare and is typically closed using a Spectralon plug. The total port area is less than 5% of the total surface area of the sphere. It is important to have the radiation balance established inside the sphere after as few internal reflections as possible. The light intensity incident on the detector should correspond to the average light intensity inside the sphere. The sphere is provided with an interior baffle to assure that the detector will not view radiation reflected directly from the sample.

## 5. Results and Discussion

The analysis of radiometric tarp samples BRDF is presented for normal and nonnormal angles of incidence. The measured BRDF has been fitted using a fifth-degree polynomial regression:

$$Y = A + Bx + Cx^2 + Dx^3 + Ex^4 + Fx^5 \qquad (5)$$

where $x$ is the scatter zenith angle or $\Theta_s$, $Y$ is the BRDF ($\Theta_s$), and $A$, $B$, $C$, $D$, $E$, and $F$ are the polynomial coefficients. The coefficients, $A$, $B$, $C$, $D$, $E$, and $F$, given in the Appendix Tables 5–7, were calculated at 485 nm wavelength, at scatter azimuth angles of 0°, 45°, 90°, 135°, and 180°, with incident angles of 0°, 10°, and 30°, and scatter zenith angles from −60° to 60°. The polynomial regression can be used for deriving BRDF data at random scatter zenith angles, $\Theta_s$, for the above-mentioned scatter azimuth and incident angles. The performance was evaluated by the root mean square error (RMSE), the most commonly used measure of success of numeric prediction. The error has the same dimensions as the predicted values themselves. The RMSE criterion is

$$\sigma = \sqrt{\frac{1}{N} \sum (f' - f)^2}, \qquad (6)$$

where $f'$ is the modeled, $f$ is the measured BRDF, and $N$ is the number of points measured.

The tarps were studied first at normal incidence, the BRDF was measured at 0°, 45°, 90°, 135°, and

Table 2.  BRDF Difference from a Reference[a] Measured at Corresponding Scatter Zenith and Azimuth Angles[b]

| Scatter Zenith | Scatter Azimuth | | | | |
|---|---|---|---|---|---|
| | 0° | 45° | 90° | 135° | 180° |
| 5 | 13.02% | | | | 13.35% |
| 10 | 8.28% | 9.70% | 11.17% | 10.59% | 9.10% |
| 15 | 5.66% | 6.58% | 7.58% | 7.25% | 5.98% |
| 20 | 3.22% | 3.85% | 4.77% | 4.50% | 3.53% |
| 25 | 1.52% | 2.08% | 2.44% | 2.12% | 1.82% |
| 30 | 0.00% | 0.00% | 0.00% | 0.00% | 0.00% |
| 35 | −1.51% | −1.54% | −1.91% | −1.90% | −1.52% |
| 40 | −2.75% | −3.13% | −3.63% | −3.53% | −2.77% |
| 45 | −3.70% | −4.77% | −5.34% | −5.29% | −4.05% |
| 50 | −4.99% | −6.19% | −7.10% | −6.68% | −5.04% |
| 55 | −5.98% | −7.57% | −8.56% | −7.75% | −6.04% |
| 60 | −6.65% | −8.28% | −10.06% | −8.84% | −7.06% |

[a]BRDF at 30° scatter zenith.
[b]Normal incidence, sample 1, 485 nm.

180° scatter azimuth angles. The scatter zenith angles vary from 10° to 60° in 5° steps. The scatter zenith angle of 0° was not measured as, at this geometry, the detector is obscured by the last fold mirror. The BRDF at normal incidence of all tarp samples at a wavelength of 485 nm is shown in Fig. 5 for scatter azimuth angles 0° and 180°. The scatter zenith angles at 0° scatter azimuth angle are presented in this figure as negative in order to be in accordance with the standard angular convention. In the following discussions, we will refer only to sample 1, as there are no substantial differences between the samples except their absolute reflectance.

The BRDF of sample 1 at 485 nm and the study scatter azimuth angles is shown in Fig. 6 as a function of scatter zenith angle at normal incidence illumination. The measurements at 550, 633 and 800 nm are not represented as they show the same tendencies and would be redundant. Two types of data are presented in Fig. 6—the fitted BRDF as plotted from the polynomial coefficients in Table 5 and the measured data points. The RMSE criterion has been used to calculate the error between the fitted and experimental data. The values for the study scatter azimuth angles, both normal and nonnormal incidence, are given in Table 5 for sample 1 at 485 nm. The largest error at normal incidence is $2.32 \times 10^{-4}$.

The surfaces of the tarp samples are structured; therefore even at normal incidence their BRDF depends on the weft and warp thread orientation. The scatter from the surface depends mainly on the scatter zenith angle. However, the warp bumps

Table 1.  Root-Mean-Square Error[a]

| Incident Angle | Scatter Azimuth | | | | |
|---|---|---|---|---|---|
| | 0° | 45° | 90° | 135° | 180° |
| 0° | $2.32 \times 10^{-4}$ | $1.37 \times 10^{-4}$ | $1.20^{-4}$ | $6.87 \times 10^{-5}$ | $8.88 \times 10^{-5}$ | |
| 10° | $1.53 \times 10^{-04}$ | $2.06 \times 10^{-04}$ | $1.73 \times 10^{-04}$ | $2.86 \times 10^{-04}$ | $1.60 \times 10^{-04}$ | |
| 30° | $1.81 \times 10^{-04}$ | $1.71 \times 10^{-04}$ | $1.85 \times 10^{-04}$ | $1.98 \times 10^{-04}$ | $1.22 \times 10^{-13}$ | $6.78 \times 10^{-09}$ |

[a]sr$^{-1}$, sample 1, 485 nm

**Table 3. BRDF Difference at Scatter Azimuth 0° versus 90°[a]**

| Scatter Zenith | 485 nm | 550 nm | 633 nm | 800 nm |
|---|---|---|---|---|
| | | Normal Incidence | | |
| 10° | −2.00% | −1.74% | −1.17% | −1.29% |
| 15° | −2.89% | −2.32% | −2.16% | −2.02% |
| 20° | −3.34% | −2.82% | −2.95% | −2.35% |
| 25° | −4.03% | −3.86% | −3.37% | −2.74% |
| 30° | −4.85% | −4.06% | −4.04% | −3.39% |
| 35° | −5.26% | −4.57% | −4.70% | −3.72% |
| 40° | −5.74% | −5.28% | −4.88% | −4.20% |
| 45° | −6.33% | −5.90% | −5.42% | −4.87% |
| 50° | −6.94% | −6.31% | −5.70% | −4.71% |
| 55° | −7.37% | −6.70% | −6.59% | −5.05% |
| 60° | −7.99% | −7.10% | −6.64% | −5.40% |
| | | 10° incident angle | | |
| 0° | 0.00% | 0.00% | 0.14% | 0.00% |
| 5° | −2.06% | −1.69% | −1.41% | −1.77% |
| 15° | −5.57% | −4.97% | −4.51% | −4.02% |
| 20° | −4.68% | −4.01% | −3.72% | −3.22% |
| 25° | −4.91% | −4.13% | −3.79% | −3.09% |
| 30° | −5.18% | −4.19% | −4.15% | −3.49% |
| 35° | −5.59% | −4.90% | −4.20% | −3.80% |
| 40° | −5.91% | −5.12% | −4.72% | −4.14% |
| 45° | −6.64% | −6.24% | −5.42% | −4.79% |
| 50° | −6.89% | −6.10% | −5.63% | −4.82% |
| 55° | −7.82% | −7.01% | −6.58% | −5.65% |
| 60° | −8.24% | −6.89% | −6.59% | −5.66% |
| | | 30° incident angle | | |
| 0° | 0.00% | 0.00% | −0.18% | −0.15% |
| 5° | −0.03% | 0.12% | 0.18% | 0.15% |
| 10° | −0.94% | −0.48% | −0.42% | −0.70% |
| 15° | −2.63% | −1.98% | −2.12% | −1.76% |
| 20° | −5.75% | −4.76% | −4.12% | −3.98% |
| 25° | −10.51% | −8.82% | −7.98% | −7.01% |
| 35° | −13.46% | −11.60% | −11.06% | −9.71% |
| 40° | −11.76% | −9.82% | −9.11% | −8.26% |
| 45° | −11.56% | −9.57% | −9.01% | −8.46% |
| 50° | −11.34% | −9.82% | −9.22% | −8.63% |
| 55° | −11.42% | −10.12% | −9.44% | −9.15% |
| 60° | −12.04% | −11.03% | −10.30% | −9.80% |

[a]%, sample 1, 90° is the base.

obscure the detector from viewing the full surface. Therefore the scatter also depends on the scatter azimuth angle whether the detector scan plane is per-
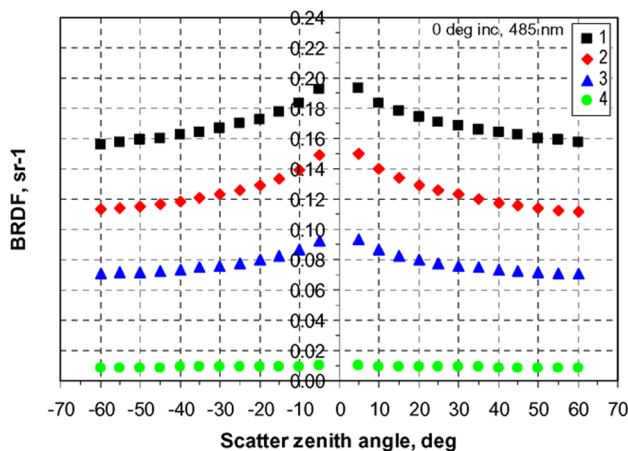


Fig. 5. (Color online) In-plane BRDF of tarps 1 to 4 at normal incidence, 485 nm, 0° and 180° scatter azimuth angle.
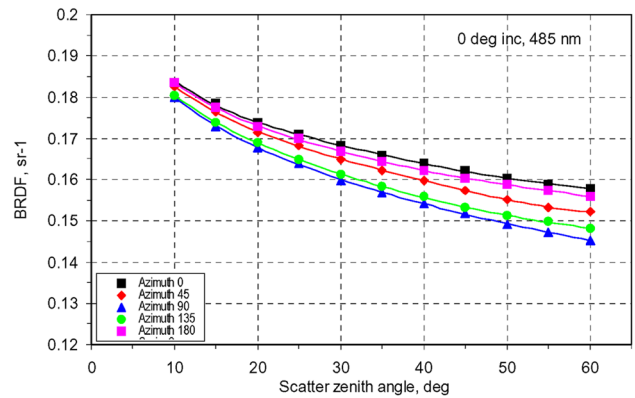


Fig. 6. (Color online) BRDF of tarp 1 at normal incidence, at different scatter azimuth angles, 485 nm, fitting and experimental points.

pendicular or not to the weft threads, Fig. 4. The BRDF is higher where the weft threads lie parallel to the detector scan plane; $X$–$Z$ plane as then the obscuration is minimal. The maximum obscuration occurs where the detector scan plane is parallel to the warp bumps, corresponding to the lower BRDF; $Y$–$Z$ plane. The obscuration effect also depends on the scatter zenith angle. It is higher at larger scatter zenith angles. In addition to the obscuration, a shadowing effect takes place at nonnormal incident angles. Both the obscuration and shadowing effects are shown schematically in Fig. 7. The highest BRDF of tarp 1 was recorded at 0° and 180° scatter azimuth where the tarp weft threads lie parallel to the detector scan plane. The BRDF decreases at 45° and 135° scatter azimuth angles as the detector rotates to an orientation 45° relative to the sample warp bumps. The lowest BRDF was measured at 90° scatter azimuth, in accordance with our expectations.

The data in Table 2 show what differences the observer should expect for airborne measurements depending on the scatter zenith angle assuming that the source (Sun) is at zenith. The data in Table 2 represent the deviation in the tarp optical scattering from Lambertian. To make the comparison simpler, we designate the BRDF at 30° scatter zenith as a reference and compare the BRDF at other scatter zenith angles to the 30° value. The BRDF differences were calculated from the BRDF data of sample 1 at 485 nm, normal incidence, and at scatter azimuth
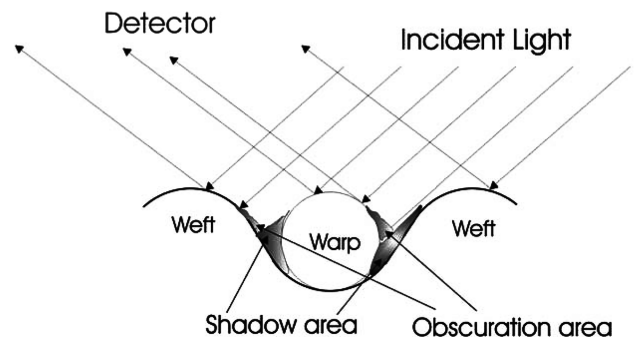


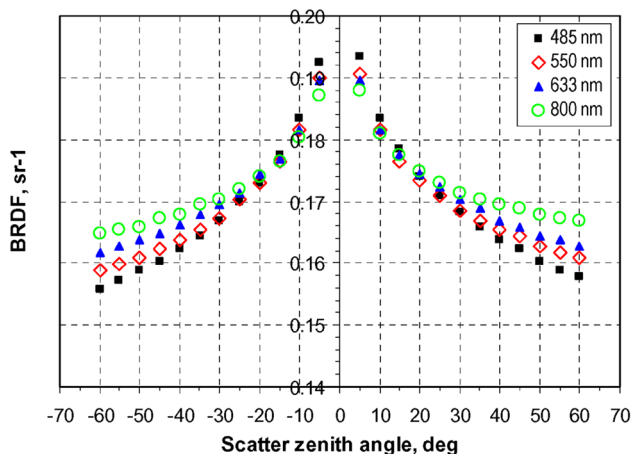Fig. 7. Shadowing and obscuration effects of tarps.

Fig. 8. (Color online) BRDF of tarp 1 at normal incidence, 485, 550, 633, and 800 nm, 0° and 180° scatter azimuth angle.

angles of 0°, 45°, 90°, 135°, and 180°. It was found that the difference could be as high as 13% for a 5° scatter zenith angle. The BRDF difference on the scatter zenith angle decreases as the wavelength increases. For example, the difference between BRDF at 30° and 5° scatter zenith is 13.02% at 485 nm and 8.83% at 800 nm. The difference between the BRDF at 30° and 60° scatter zenith is −6.65% at 485 nm increasing to 2.76% at 800 nm.

The dependence of BRDF on wavelength at normal incidence for sample 1 is given in Fig. 8 at 485, 550, 633, and 800 nm and at scatter azimuths of 0° and 180°. The BRDF does not change at small scatter zenith angles, while at larger scatter zenith angles the BRDF increases with the wavelength. The detector scan plane is parallel to the weft threads at scatter azimuth angles of 0° and 180° and perpendicular to them at a scatter azimuth angle of 90°. The BRDF dependence on the weft threads is best addressed when the BRDF at scatter azimuth angles of 0° and 90° are compared. For this comparison, the weft threads influence is presented in Table 3 for sample 1 at wavelengths of 485, 550, and 633 nm. Although this section only discusses the data related normal incidence, Table 3 includes the nonnormal incidence data as well. The BRDF obtained at nonnormal incidence is addressed in the respective section. The BRDF measured at a scatter azimuth of 90° is used as a reference. Since the BRDF at 0° is always higher than at 90°, the data in Table 3 are negative. The difference at normal incidence could be as high as −7.99% at 60° scatter zenith at 485 nm and as low as −1.17% at 10° scatter zenith at 633 nm. The difference in BRDF at 0° versus 90° increases with scatter zenith angle for all wavelengths at normal incidence. It is also higher at shorter wavelengths. Although not presented, the results of samples 2, 3, and 4 show the same characteristics. The variation in BRDF is due to the warp bumps obscuring effect translated into the data at normal incidence.

The BRDF of the tarp samples at nonnormal incident angles is different from that at normal incidence. The difference is mainly due to the nonisotropic structure of the sample's surface. The warp bumps (i) partially obscure the detector view and (ii) shadow a portion of the illuminated area of the sample. The two effects reduce the observed BRDF. The influence of these effects on BRDF depends on the incident angle, scatter zenith and azimuth angles, and the orientation of the weft threads relative to the plane of the incident light.

In the process of characterizing the sample BRDF, we fitted the measured points using a standard polynomial procedure, similar to what we used at normal incidence. The coefficients of the polynomial regression are given in Tables 6 and 7 according to the wavelength and measurement geometry for 10° and 30° incident angles. The polynomial regression can be used for deriving BRDF data at random scatter zenith angles at fixed scatter azimuth angles. The fitting procedure was applied for scatter zenith angles from 0° to 60°, except at the 180° scatter azimuth where it was applied from 15° to 60° due to the detector obscuration at 10° scatter zenith. Two polynomials were used to model the BRDF at the 30° incident angle geometry, one for 0° to 25° scatter zenith and one for 35° to 60° scatter zenith as the detector is obscured at the 30° scatter zenith angle.

***BRDF versus scatter zenith angle***. BRDF data were acquired at 10° and 30° incident angles for 0°, 45°, 90°, 135°, and 180° scatter azimuth positions on all samples. The scatter zenith angles vary from 0° to 60° in 5° steps. The BRDF of sample 1 at 485 nm is presented in Figs. 9 and 10 for 10° and 30° incident angles, respectively. The BRDF of samples 2, 3, and 4 as well as the measurements at 550, 633, and 800 nm are not presented as they show the same scattering tendencies. Two types of data are presented in the figures—the fitted BRDF curve and the measured points. The fitted curves are plotted from the polynomial coefficients as given in Table 6 for 10° and Table 7 for 30° incident angles. The BRDF at 10° incidence angle was seen to decrease to a different extent with increasing scatter zenith angle for 0°, 45°, and 90° scatter azimuth independently of wavelength for all samples. The BRDF data at 180° scat-
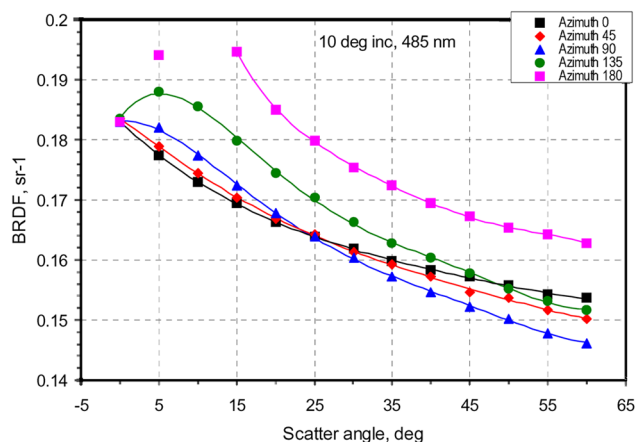


Fig. 9. (Color online) BRDF of tarp 1 at 10° incidence at different scatter azimuth angles, 485 nm, fitting and experimental points.
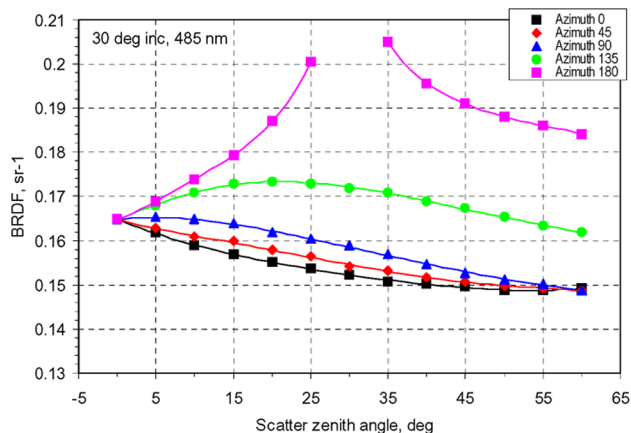
Fig. 10. (Color online) BRDF of tarp 1 at 30° incidence at different scatter azimuth angles, 485 nm, fitting and experimental points.

ter azimuth follow the tendency as discussed for the case of normal incidence. The BRDF in the principal plane is higher at scatter zenith angles closest to the angle of incidence. The BRDF at 135° scatter azimuth follows the same pattern although the BRDF values are lower than those measured at 180° scatter azimuth. Figure 10 shows the BRDF at 30° incident angle and 485 nm for 0°, 45°, 90°, 135°, and 180° scatter azimuth. The BRDF follows the same pattern as at the 10° incident angle. However the BRDF at 180° scatter azimuth is significantly higher than the BRDF at other scatter azimuth angles and at smaller scatter zenith angles.

The BRDF dependence on the weft threads is best represented by comparing the BRDF at scatter azimuth angles of 0° and 90°. The difference in BRDF of sample 1 at a scatter azimuth 0° versus the BRDF at a scatter azimuth of 90° is presented in Table 3 at 485, 550, 633, 800 nm, summarizing data for both normal and nonnormal incidence. The BRDF measured at a scatter azimuth of 90° is used as a reference. Since the BRDF at scatter azimuth 0° is always higher than at scatter azimuth 90°, the data in Table 3 are negative. The difference at 30° incident an-
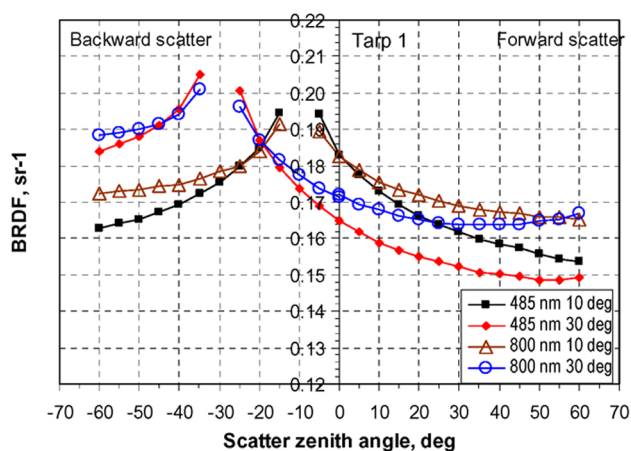
gle could be as high as –12% at 60° scatter zenith and as low as 0% at 0° scatter zenith both at 485 nm.

**Backward and forward scatter.** The BRDF at nonnormal incidence provides information on the forward and backward scattering properties of the tarps. We are considering the BRDF to be in the forward direction when the detector is positioned opposite the light source. The backward scatter takes place when the detector is positioned back toward the light source. The typical BRDF has a maximum at the retroscatter position occurring when the detector is aligned on the same line with the source and the sample. The cause of the maximum BRDF is the hiding of shadows and obscuration effects at this geometry. The forward and backward scatters are compared by simply looking at the difference of the BRDF at scatter zenith angles symmetric to the source zenith position. Tarps 1, 2, and 3, called white tarps hereafter, exhibit well-pronounced backward scattering, better expressed at larger incident angles for both 10° and 30° incident angles as shown for tarp 1 in Fig. 11. The white tarps' backward scattering is better pronounced at shorter wavelengths. However the scattering of tarp 4, the black tarp, is quite different. This sample has well-pronounced forward scattering properties as shown in Fig. 12, especially at 30° incident angle. The forward scattering is also apparent for scatter zenith greater than 25° angles and at 10° incidence angle.

It is not unusual for black materials to have different scatter distributions than white materials. The tarps used in remote sensing calibrations are generally treated with a pigment of titanium dioxide and carbon black and coated with a silicone pigment. The carbon black exhibits strong forward scattering properties [19]. We believe the forward scattering properties demonstrated by the black sample are due to the carbon black used at the manufacturing process and its polarization properties.

**BRDF spectral dependence.** The BRDF spectral dependence based on data measured at wavelengths of 485, 550, 633, and 800 nm is shown in Fig. 13. The
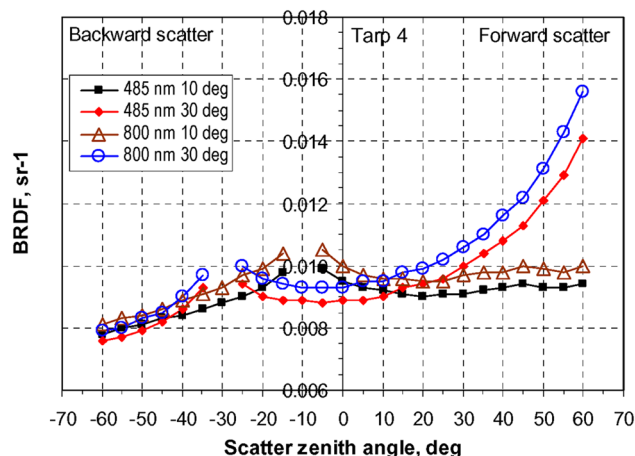


Fig. 11. (Color online) Forward–backward scatter, tarp 1, 485 and 800 nm, 10° and 30° incident angle.



Fig. 12. (Color online) Forward–backward scatter, tarp 4, 485 and 800 nm, 10° and 30° incident angle.

BRDF of tarp 1 at incident angle 30°, at scatter azimuth angles of 0° and 180°, is presented for scatter zenith angles from 0° to 60°, in 10° steps. The BRDF spectral dependence at nonnormal incidence follows the same pattern as at normal incidence, that is, the BRDF increases with the wavelength. All the samples were found to have the same spectral dependence, including the black sample. However, the BRDF data of the black sample in the visible (485, 550, and 633 nm) were very similar, only the BRDF at 800 nm being higher. This makes the black sample BRDF properties spectrally indifferent in the visible range.

**8° directional/hemispherical measurement.** The 8° directional/hemispherical reflectance of all the tarp samples was measured with a He–Ne laser at 632.8 nm. The only hardware difference from the experimental setup described in the Section 3 is the use of an 8° directional/hemispherical integrating sphere mounted above the scatterometer sample stage. The silicon photodiode detector was fixed to one port of the sphere. The relationship between sample reflectance and detector signal can be parameterized using Spectralon samples of known reflectance. We chose a 3rd order polynomial for this parameterization. The coefficients of the polynomial were calculated by fitting the receiver power measured with a set of seven gray Spectralon standard targets of nominal reflectance 5%, 10%, 20%, 40%, 60%, 80%, and 99% with known 8° directional/hemispherical reflectance. The measured 8° directional/hemispherical reflectance data for each sample are given in Table 4.

## 6. Conclusions

The BRDF results of four radiometric tarp samples calibrated at NASA's GSFC Diffuse Calibration Facility show a strong dependence on the weave orientation relative to the measurement geometry. The experimental data show that the weft and warp thread orientation has a clear effect on BRDF for both normal and nonnormal incident angles. Nonnor-
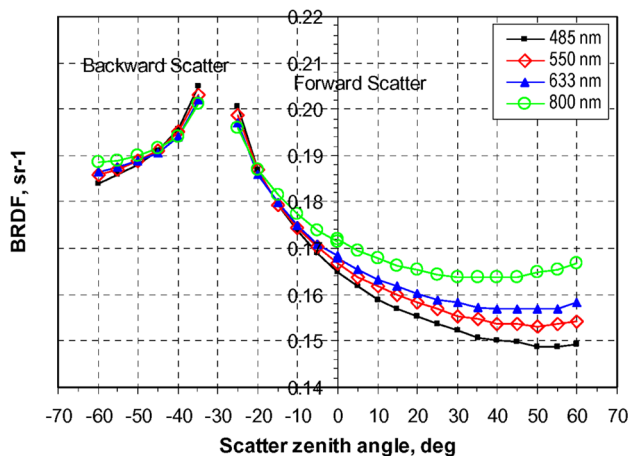
**Table 4. 8° Directional/Hemispherical Reflectance at 632.8 nm**

| Sample | Hemispherical Reflectance |
|--------|---------------------------|
| 1 | 67.34% |
| 2 | 49.65% |
| 3 | 31.93% |
| 4 | 4.35% |

mal incident angles introduce an additional dependence of BRDF on weave orientation. BRDF differences vary and can approach 12% for nonnormal incidence and 8% for normal incident angle. There is also a spectral dependence on BRDF, which is apparent at higher scatter zenith angles over the spectral range from 485 to 800 nm for both normal and nonnormal incidence. The fitted BRDF values show a very small discrepancies from the measured ones in both normal and nonnormal incident angles. The highest RMSE was calculated to be $2.32 \times 10^{-4} \text{sr}^{-1}$. The provided polynomial coefficients can be used for calculating the BRDF at random scatter zenith angles. The forward and backward scatter properties of the tarps were also studied. The backward scatter is well pronounced for the white samples—tarps 1, 2, and 3. Tarp 4, the black sample, has well-pronounced forward scatter. The forward scatter is most likely induced by carbon black used in the manufacturing of the darkest sample and its scatter polarization properties. The 8° directional/hemispherical reflectance data complement the BRDF measurements.

The current study provides the remote sensing community with important high-accuracy BRDF calibration data of radiometric tarps used in the vicarious calibrations of satellite instruments. The BRDF data obtained from these studies are important for future NASA SSC vicarious calibrations through analysis of the BRDF dependence on weft and warp thread orientation. The BRDF characterization methodologies of tarp samples as shown in this paper can be successfully extended to other structured surface fabric samples.

Fig. 13.  (Color online) Tarp sample 1 at 30° incidence, 485 nm, 550 nm, 633 nm, and 800 nm.

## Appendix A

The numerical values of polynomial coefficients, *A*, *B*, *C*, *D*, *E*, and *F* are given in Tables 5–7:

**Table 5. Polynomial Coefficients of the Samples at Normal Incidence, 485 nm**

| Coefficients | Scatter Azimuth | | | | |
|---|---|---|---|---|---|
| | **Sample 1** | | | | |
| | 0° | 45° | 90° | 135° | 180° |
| A | 0.20825 | 0.20184 | 0.20172 | 0.20113 | 0.20614 |
| B | $-3.69548 \times 10^{-3}$ | $-2.52895 \times 10^{-3}$ | $-2.95644 \times 10^{-3}$ | $-2.80741 \times 10^{-3}$ | $-3.32718 \times 10^{-3}$ |
| C | $1.63404 \times 10^{-4}$ | $6.91565 \times 10^{-5}$ | $9.51081 \times 10^{-5}$ | $9.11978 \times 10^{-5}$ | $1.36292 \times 10^{-4}$ |
| D | $-4.18955 \times 10^{-6}$ | $-9.95396 \times 10^{-7}$ | $-2.02885 \times 10^{-6}$ | $-1.99668 \times 10^{-6}$ | $-3.43818 \times 10^{-6}$ |
| E | $5.37358 \times 10^{-8}$ | $3.71795 \times 10^{-9}$ | $2.31818 \times 10^{-8}$ | $2.33217 \times 10^{-8}$ | $4.48814 \times 10^{-8}$ |
| F | $-2.68175 \times 10^{-10}$ | $2.5641 \times 10^{-11}$ | $-1.07692 \times 10^{-10}$ | $-1.07692 \times 10^{-10}$ | $-2.31976 \times 10^{-10}$ |
| | **Sample 2** | | | | |
| A | 0.16405 | 0.16329 | 0.15781 | 0.16607 | 0.16417 |
| B | $-3.52082 \times 10^{-3}$ | $-3.80467 \times 10^{-3}$ | $-2.95437 \times 10^{-3}$ | $-4.54988 \times 10^{-3}$ | $-3.73089 \times 10^{-3}$ |
| C | $1.41832 \times 10^{-4}$ | $1.67633 \times 10^{-4}$ | $9.67351 \times 10^{-5}$ | $2.19402 \times 10^{-4}$ | $1.62164 \times 10^{-4}$ |
| D | $-3.40202 \times 10^{-6}$ | $-4.48153 \times 10^{-6}$ | $-2.16148 \times 10^{-6}$ | $-6.30198 \times 10^{-6}$ | $-4.10819 \times 10^{-6}$ |
| E | $4.10483 \times 10^{-8}$ | $6.01981 \times 10^{-8}$ | $2.6352 \times 10^{-8}$ | $9.06993 \times 10^{-8}$ | $5.18333 \times 10^{-8}$ |
| F | $-1.91855 \times 10^{-10}$ | $-3.12821 \times 10^{-10}$ | $-1.28205 \times 10^{-10}$ | $-5.02564 \times 10^{-10}$ | $-2.5098 \times 10^{-10}$ |
| | **Sample 3** | | | | |
| A | 0.10311 | 0.0977 | 0.0995 | 0.0974 | 0.10218 |
| B | $-2.38324 \times 10^{-3}$ | $-1.55687 \times 10^{-3}$ | $-2.07108 \times 10^{-3}$ | $-1.61648 \times 10^{-3}$ | $-2.29836 \times 10^{-3}$ |
| C | $9.63805 \times 10^{-5}$ | $4.05597 \times 10^{-5}$ | $6.94231 \times 10^{-5}$ | $4.15026 \times 10^{-5}$ | $9.2933 \times 10^{-5}$ |
| D | $-2.25495 \times 10^{-6}$ | $-6.38753 \times 10^{-7}$ | $-1.5035 \times 10^{-6}$ | $-6.49476 \times 10^{-7}$ | $-2.1905 \times 10^{-6}$ |
| E | $2.69601 \times 10^{-8}$ | $5.20979 \times 10^{-9}$ | $1.7669 \times 10^{-8}$ | $5.34965 \times 10^{-9}$ | $2.65967 \times 10^{-8}$ |
| F | $-1.26998 \times 10^{-10}$ | $-1.53846 \times 10^{-11}$ | $-8.20513 \times 10^{-11}$ | $-1.53846 \times 10^{-11}$ | $-1.28205 \times 10^{-10}$ |
| | **Sample 4** | | | | |
| A | 0.01092 | 0.01005 | $8.46818 \times 10^{-3}$ | $9.39545 \times 10^{-3}$ | 0.01039 |
| B | $-2.41551 \times 10^{-4}$ | $-1.29779 \times 10^{-5}$ | $2.42244 \times 10^{-4}$ | $5.50635 \times 10^{-5}$ | $-1.08233 \times 10^{-4}$ |
| C | $1.3284 \times 10^{-5}$ | $-7.4528 \times 10^{-6}$ | $-2.24962 \times 10^{-5}$ | $-9.82197 \times 10^{-6}$ | $1.75257 \times 10^{-6}$ |
| D | $-3.65361 \times 10^{-7}$ | $3.98485 \times 10^{-7}$ | $7.69172 \times 10^{-7}$ | $3.85839 \times 10^{-7}$ | $5.11758 \times 10^{-8}$ |
| E | $4.59345 \times 10^{-9}$ | $-7.71562 \times 10^{-9}$ | $-1.16667 \times 10^{-8}$ | $-6.18881 \times 10^{-9}$ | $-2.0074 \times 10^{-9}$ |
| F | $-2.14178 \times 10^{-11}$ | $5.12821 \times 10^{-11}$ | $6.66667 \times 10^{-11}$ | $3.58974 \times 10^{-11}$ | $1.71946 \times 10^{-11}$ |

**Table 6. Polynomial Coefficients of the Samples at 10° Incidence, 485 nm**

| Coefficients | Scatter Azimuth | | | | |
|---|---|---|---|---|---|
| | **Sample 1** | | | | |
| | 0° | 45° | 90° | 135° | 180° |
| A | 0.18296 | 0.18354 | 0.18312 | 0.18365 | 0.28976 |
| B | $-1.20021 \times 10^{-3}$ | $-9.69627 \times 10^{-4}$ | $1.11966 \times 10^{-4}$ | $1.74708 \times 10^{-3}$ | $-0.01248$ |
| C | $2.15828 \times 10^{-5}$ | $2.51107 \times 10^{-6}$ | $-9.95822 \times 10^{-5}$ | $-2.2565 \times 10^{-4}$ | $5.94409 \times 10^{-4}$ |
| D | $-1.37951 \times 10^{-7}$ | $3.74383 \times 10^{-7}$ | $3.87859 \times 10^{-6}$ | $7.98647 \times 10^{-6}$ | $-1.5002 \times 10^{-5}$ |
| E | $-1.79899 \times 10^{-9}$ | $-8.2586 \times 10^{-9}$ | $-6.19032 \times 10^{-8}$ | $-1.23052 \times 10^{-7}$ | $1.88765 \times 10^{-7}$ |
| F | $2.32278 \times 10^{-11}$ | $5.3997 \times 10^{-11}$ | $3.59276 \times 10^{-10}$ | $7.01357 \times 10^{-10}$ | $-9.31282 \times 10^{-10}$ |
| | **Sample 2** | | | | |
| A | 0.13859 | 0.13867 | 0.13873 | 0.13875 | 0.24535 |
| B | $-1.36321 \times 10^{-3}$ | $-9.63364 \times 10^{-4}$ | $-2.23778 \times 10^{-4}$ | $1.74996 \times 10^{-3}$ | $-0.01204$ |
| C | $3.90652 \times 10^{-5}$ | $-2.29028 \times 10^{-6}$ | $-6.973 \times 10^{-5}$ | $-2.19264 \times 10^{-4}$ | $5.41148 \times 10^{-4}$ |
| D | $-9.58556 \times 10^{-7}$ | $5.30793 \times 10^{-7}$ | $2.82008 \times 10^{-6}$ | $7.65497 \times 10^{-6}$ | $-1.26653 \times 10^{-5}$ |
| E | $1.33374 \times 10^{-8}$ | $-1.02153 \times 10^{-8}$ | $-4.4891 \times 10^{-8}$ | $-1.16757 \times 10^{-7}$ | $1.46154 \times 10^{-7}$ |
| F | $-7.30015 \times 10^{-11}$ | $6.36501 \times 10^{-11}$ | $2.6003 \times 10^{-10}$ | $6.61538 \times 10^{-10}$ | $-6.5641 \times 10^{-10}$ |
| | **Sample 3** | | | | |
| A | 0.08608 | 0.08612 | 0.08621 | 0.08609 | 0.14903 |
| B | $-9.23378 \times 10^{-4}$ | $-6.93915 \times 10^{-4}$ | $-1.81439 \times 10^{-4}$ | $1.09972 \times 10^{-3}$ | $-6.82608 \times 10^{-3}$ |
| C | $2.54172 \times 10^{-5}$ | $1.76028 \times 10^{-6}$ | $-4.5006 \times 10^{-5}$ | $-1.40507 \times 10^{-4}$ | $2.94509 \times 10^{-4}$ |
| D | $-4.75932 \times 10^{-7}$ | $3.40265 \times 10^{-7}$ | $1.89407 \times 10^{-6}$ | $4.89841 \times 10^{-6}$ | $-6.80331 \times 10^{-6}$ |
| E | $5.38599 \times 10^{-9}$ | $-7.49074 \times 10^{-9}$ | $-3.05882 \times 10^{-8}$ | $-7.39696 \times 10^{-8}$ | $7.92075 \times 10^{-8}$ |
| F | $-2.62443 \times 10^{-11}$ | $5.12821 \times 10^{-11}$ | $1.79487 \times 10^{-10}$ | $4.14178 \times 10^{-10}$ | $-3.65128 \times 10^{-10}$ |
| | **Sample 4** | | | | |
| A | $9.48484 \times 10^{-3}$ | $9.48213 \times 10^{-3}$ | $9.51946 \times 10^{-3}$ | $9.50271 \times 10^{-3}$ | 0.01512 |
| B | $-1.9931 \times 10^{-5}$ | $-1.30863 \times 10^{-5}$ | $-2.16218 \times 10^{-5}$ | $6.22498 \times 10^{-5}$ | $-7.10272 \times 10^{-5}$ |
| C | $-2.58155 \times 10^{-6}$ | $-3.54336 \times 10^{-6}$ | $-2.97816 \times 10^{-6}$ | $-1.06857 \times 10^{-5}$ | $3.47308 \times 10^{-5}$ |
| D | $1.91907 \times 10^{-7}$ | $2.05142 \times 10^{-7}$ | $1.17267 \times 10^{-7}$ | $4.06767 \times 10^{-7}$ | $-8.93986 \times 10^{-7}$ |
| E | $-4.0436 \times 10^{-9}$ | $-3.96682 \times 10^{-9}$ | $-1.6221 \times 10^{-9}$ | $-6.59948 \times 10^{-9}$ | $1.14219 \times 10^{-8}$ |
| F | $2.7451 \times 10^{-11}$ | $2.6546 \times 10^{-11}$ | $8.74811 \times 10^{-12}$ | $3.92157 \times 10^{-11}$ | $-5.74359 \times 10^{-11}$ |

| Coefficients | Scatter Azimuth | | | | | |
|---|---|---|---|---|---|---|
| | 0° | 45° | 90° | 135° | 180° | |
| | Scatter zenith | | | | 0° to 45° | 35° to 60° |
| *Sample 1* | | | | | | |
| A | 0.16484 | 0.16479 | 0.16483 | 0.16467 | 0.1648 | 2.6852 |
| B | $-7.09245 \times 10^{-4}$ | $-4.62207 \times 10^{-4}$ | $2.03307 \times 10^{-4}$ | $7.44778 \times 10^{-4}$ | $6.15333 \times 10^{-4}$ | $-0.24781$ |
| C | $1.45158 \times 10^{-5}$ | $1.4295 \times 10^{-5}$ | $2.61323 \times 10^{-5}$ | $-7.18017 \times 10^{-6}$ | $5.76667 \times 10^{-5}$ | $9.959 \times 10^{-3}$ |
| D | $1.93459 \times 10^{-7}$ | $-6.41475 \times 10^{-7}$ | $5.84595 \times 10^{-7}$ | $7.11261 \times 10^{-7}$ | $-3.83333 \times 10^{-6}$ | $-2.01367 \times 10^{-4}$ |
| E | $7.59633 \times 10^{-10}$ | $1.23776 \times 10^{-8}$ | $-6.8696 \times 10^{-9}$ | $1.65611 \times 10^{-8}$ | $9.33333 \times 10^{-8}$ | $2.04 \times 10^{-6}$ |
| F | $8.44646 \times 10^{-12}$ | $-7.93364 \times 10^{-11}$ | $3.68024 \times 10^{-11}$ | $-1.06486 \times 10^{-10}$ | $8 \times 10^{-10}$ | $-8.26667 \times 10^{-9}$ |
| *Sample 2* | | | | | | |
| A | 0.1226 | 0.12245 | 0.12244 | 0.12249 | 0.1225 | 2.5561 |
| B | $-7.37016 \times 10^{-4}$ | $-3.02171 \times 10^{-4}$ | $1.98946 \times 10^{-4}$ | $6.47981 \times 10^{-4}$ | $3.90333 \times 10^{-4}$ | $-0.23511$ |
| C | $1.38939 \times 10^{-5}$ | $-1.48631 \times 10^{-5}$ | $-3.30949 \times 10^{-5}$ | $-4.34286 \times 10^{-6}$ | $1.34167 \times 10^{-4}$ | $9.2725 \times 10^{-3}$ |
| D | $-1.89946 \times 10^{-7}$ | $6.02033 \times 10^{-7}$ | $8.51464 \times 10^{-7}$ | $-7.23382 \times 10^{-7}$ | $-1.30333 \times 10^{-5}$ | $-1.837 \times 10^{-4}$ |
| E | $7.65117 \times 10^{-10}$ | $-8.85918 \times 10^{-9}$ | $-1.02797 \times 10^{-8}$ | $1.55492 \times 10^{-8}$ | $5.53333 \times 10^{-7}$ | $1.82 \times 10^{-6}$ |
| F | $8.74811 \times 10^{-12}$ | $4.97738 \times 10^{-11}$ | $5.33937 \times 10^{-11}$ | $-9.2006 \times 10^{11-11}$ | $-7.2 \times 10^{-9}$ | $-7.2 \times 10^{-9}$ |
| *Sample 3* | | | | | | |
| A | 0.07348 | 0.0735 | 0.07351 | 0.0735 | 0.0735 | 1.4191 |
| B | $-4.83623 \times 10^{-4}$ | $-2.90567 \times 10^{-4}$ | $6.10769 \times 10^{-5}$ | $3.87863 \times 10^{-4}$ | $6.41333 \times 10^{-4}$ | $-0.12745$ |
| C | $8.17157 \times 10^{-6}$ | $-2.45451 \times 10^{-6}$ | $-1.10758 \times 10^{-5}$ | $3.42037 \times 10^{-6}$ | $-4.03333 \times 10^{-5}$ | $4.96017 \times 10^{-3}$ |
| D | $-1.1751 \times 10^{-8}$ | $2.9118 \times 10^{-7}$ | $3.14452 \times 10^{-7}$ | $-3.62923 \times 10^{-7}$ | $6.2 \times 10^{-6}$ | $-9.72 \times 10^{-5}$ |
| E | $-1.3177 \times 10^{-9}$ | $-5.86727 \times 10^{-9}$ | $-3.9627 \times 10^{-9}$ | $4.70725 \times 10^{-9}$ | $-3.06667 \times 10^{-7}$ | $9.53333 \times 10^{-7}$ |
| F | $1.68929 \times 10^{-11}$ | $4.19306 \times 10^{-11}$ | $2.05128 \times 10^{-11}$ | $-1.56863 \times 10^{-11}$ | $5.86667 \times 10^{-9}$ | $-3.73333 \times 10^{-9}$ |
| *Sample 4* | | | | | | |
| A | $8.88778 \times 10^{-3}$ | $8.90136 \times 10^{-3}$ | $8.90407 \times 10^{-3}$ | $8.88484 \times 10^{-3}$ | $8.9 \times 10^{-3}$ | 0.1738 |
| B | $-8.611 \times 10^{-7}$ | $-2.09143 \times 10^{-5}$ | $4.48396 \times 10^{-6}$ | $-1.71592 \times 10^{-5}$ | $-1.05 \times 10^{-4}$ | $-0.01642$ |
| C | $1.76189 \times 10^{-8}$ | $5.2077 \times 10^{-7}$ | $-2.16554 \times 10^{-6}$ | $2.1775 \times 10^{-6}$ | $2.75 \times 10^{-5}$ | $6.58667 \times 10^{-4}$ |
| D | $-2.36323 \times 10^{-8}$ | $-2.6704 \times 10^{-7}$ | $9.82723 \times 10^{-8}$ | $-1.52969 \times 10^{-7}$ | $-2.56667 \times 10^{-6}$ | $-1.32667 \times 10^{-5}$ |
| E | $1.28891 \times 10^{-10}$ | $5.53819 \times 10^{-9}$ | $-1.91828 \times 10^{-9}$ | $3.03579 \times 10^{-9}$ | $1 \times 10^{-7}$ | $1.33333 \times 10^{-7}$ |
| F | $3.01659 \times 10^{-12}$ | $-3.65008 \times 10^{-11}$ | $1.44796 \times 10^{-11}$ | $-1.93062 \times 10^{-11}$ | $-1.33333 \times 10^{-9}$ | $-5.33333 \times 10^{-10}$ |

## References

1. J. J. Butler, B. C. Johnson, and R. A. Barnes, "The calibration and characterization of Earth remote sensing and environmental monitoring instruments," in *Optical Radiometry*, A. C. Parr, R. U. Datla, and J. L. Gardner, eds. (Academic, 2005).

2. G. B. Courreges-Lacoste, J. G. Schaarsberg, R. Sprik, and S. Delward, "Modeling of Spectralon diffusers for radiometric calibration in remote sensing," Opt. Eng. **42**, 3600–3607 (2003).

3. C. J. Bruegge, A. E. Stiegman, R. A. Rainen, and A. W. Springsteen, "Use of Spectralon as a diffuse reflectance standard for in-flight calibration of earth-orbiting sensors," Opt. Eng. **32**, 805–814 (1993).

4. C. K. Gatebe, M. D. King, S. Platnick, G. T. Arnold, E. F. Vermote, and B. Schmid, "Airborne spectral measurements of surface-atmosphere anisotropy for several surfaces and ecosystems over southern Africa," J. Geophys. Res. **108**, 8487 (2003).

5. C. K. Gatebe, M. D. King, A. I. Lyapustin, G. T. Arnold, and J. Redemann, "Airborne spectral measurements of ocean directional reflectance," J. Atmos. Sci. **62**, 1072–1092 (2005).

6. M. D. King, "Directional and spectral reflectance of the Kuwait oil-fire smoke," J. Geophys. Res. **97**, 14545–14549 (1992).

7. S. Blonski, M. Pagnutti, R. E. Ryan, and V. Zanoni, "In-flight edge response measurements for high-spatial-resolution remote sensing systems," Proc. SPIE **4814**, 317–326 (2002).

8. M. Pagnutti, R. Ryan, M. Kelly, K. Holekamp, V. Zanoni, K Thome, and S. Schiller, "Radiometric characterization of IKONOS multispectral imagery," Remote Sens. Environ. **88**, 53–68 (2003).

9. J. R. Proctor and P. Y. Barnes, "NIST High accuracy reference reflectometer—spectrophotometer," J. Res. Nat. Inst. Stand. Technol. **101**, 619–627 (1996).

10. F. E. Nicodemus, J. C. Richmond, J. J. Hsia, I. W. Ginsburg, and T. Limperis, "Geometrical considerations and nomenclature for reflectance," National Bureau of Standards, NBS monograph 160 Oct. 1977.

11. J. C. Stover, *Optical Scattering: Measurement and Analysis* (SPIE, 1995).

12. T. F. Schiff, M. W. Knighton, D. J. Wilson, F. M. Cady, J. C. Stover, and J. J. Butler, "Design review of a high accuracy UV to near infrared scatterometer," Proc. SPIE **1995**, 121–130 (1993).

13. F. M. Cady, D. R. Bjork, J. Rifkin, and J. C. Stover, "BRDF error analysis," Proc. SPIE **1165**, 154–164 (1989).

14. B. N. Taylor and C. E. Kuyatt, "Guidelines for Evaluating and Expressing the Uncertainty of NIST Measurement Results," NIST Technical Note 1297, U.S. Department of Commerce, National Institute of Standards and Technology, Sept. 1997.

15. E. A. Early, P. Y. Barnes, B. C. Johnson, J. J. Butler, C. J. Bruegge, S. F. Biggar, P. S. Spyak, and M. M. Pavlov, "Bidirectional reflectance round-robin in support of the Earth Observing System Program," J. Atmos. Ocean. Technol. **17**, 1077–1091 (2000).

16. G. T. Georgiev and J. J. Butler: "Long-term calibration monitoring of spectralon diffusers BRDF in the air-ultraviolet," Appl. Opt. **46**, 7892–7899 (2007).

17. G. T. Georgiev and J. J. Butler, "Bidirectional reflectance distribution function and directional/hemispherical reflectance of Martian regolith simulant," Opt. Eng. **44**, 036202 (2005).

18. G. T. Georgiev, C. K. Gatebe, J. J. Butler, and M. D. King, "Comparison between laboratory and airborne BRDF measurements for remote sensing," Proc. SPIE **6296**, 629603 (2006).

19. S. Smith and J. C. Fleming, "BRDF measurements of a new IR black coating with lower reflectance," Proc. SPIE **3426**, 333–343 (1998).